Temperature and Gate Dependence of Carrier Diffusion in Single Crystal Methylammonium Lead Iodide Perovskite Microstructures

Luke McClintock,[†] Rui Xiao,[†] Yasen Hou,[†] Clinton Gibson,[†] H. Clark Travaglini,[†] David Abramovitch,[‡,¶] Liang Z. Tan,[¶] R. Tugrul Senger,[§] Yongping Fu,[‖] Song Jin,[‖] and Dong Yu[†]

†*Department of Physics, University of California-Davis, One Shields Avenue, Davis, CA 95616*

‡*Department of Physics, University of California-Berkeley, 366 LeConte Hall, Berkeley, CA 94720*

¶*Molecular Foundry, Lawrence Berkeley Laboratory, 67 Cyclotron Rd, Berkeley, CA 94720*

§*Department of Physics, Izmir Institute of Technology, 35430 Izmir, Turkey*

‖*Department of Chemistry, University of Wisconsin-Madison, 1101 University Avenue, Madison, WI 53706*

Abstract

We investigate temperature dependent photogenerated carrier diffusion in single-crystal methylammonium lead iodide ($MAPbI_3$) microstuctures via scanning photocurrent microscopy. Carrier diffusion lengths were found to increase abruptly across the tetragonal to the orthorhombic phase transition and reached 200 $\pm$ 50 μm at 80 K. In combination with the microsecond carrier lifetime measured by a transient photocurrent method, an enormous carrier mobility value of 3 $\times$ 10^4 cm^2 / V s was extracted at 80 K. The observed highly non-local photocurrent and the rapid increase of carrier diffusion length at low temperature can be understood by formation and efficient transport of free excitons in the orthorhombic phase, as a result of reduced optical phonon scattering due to the dipolar nature of the excitons. Carrier diffusion lengths were tuned by a factor of 8 by gate voltage and increased with increasing majority carrier (electron) concentration, consistent with the exciton model.

Graphical TOC Entry

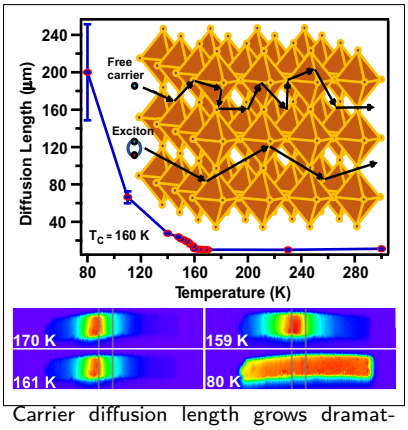

Carrier diffusion length grows dramatically after tetragonal to orthorhombic phase change, as transport becomes more excitonic in nature.

Halide perovskites exhibit ideal electronic properties, including long carrier lifetime and diffusion length, essential to their unprecedentedly rapid advancement in photovoltaic performance. While several mechanisms such as local polar fluctuation,[1] polaron formation,[2] spin-orbit coupling,[3] ion migration,[4] and ferroelectricity[5] have been proposed, the true origins are still under intense debate. Exploration of these materials at low temperature reduces complications resulting from thermal fluctuations. Carrier mobilities are shown to follow a power law dependence on temperature ($\mu \sim T^{-1.5}$) in both $MAPbI_3$[6,7] and $MAPbBr_3$,[8] consistent with phonon scattering.[9–13] Along with mobility, charge carrier diffusion length (L_{diff}) is a critical optoelectronic parameter, determined by the diffusion coefficient D and the lifetime τ of the charge carriers ($L_{diff} = \sqrt{D\tau}$), while D is related to the carrier mobility by $\mu = qD/k_BT$. L_{diff} values have been experimentally determined by separately measuring μ and τ,[14,15] or directly from spatially resolved photoluminescence[16] or photocurrent measurements.[17–20]

Here, we examine the roles that temperature and structural phase play on carrier transport and recombination within $MAPbI_3$ single crystal microstructures. We apply scanning photocurrent microscopy (SPCM) to directly extract the carrier diffusion length in $MAPbI_3$ microplate field effect transistors (FETs) in the temperature range of 80 - 300 K. Studying single crystal halide perovskites eliminates the complications caused by grain boundaries as in polycrystals. Furthermore, unlike bulk single crystals, single crystal nano- and microstructures[21] allow in-situ gate tuning of Fermi level in the material,[22] facilitating exploration of charge transport mechanisms. Single crystalline microstructures of $MAPbI_3$ are synthesized following a dissolution and recrystallization process.[23] Microbeams and microplates with thickness of about 1-2 μm and length up to 100 μm are produced with well defined facets and smooth surfaces (Figure 1a). These microstructures are mechanically transferred to pre-patterned Cr/Au electrodes on SiO_2 coated Si substrates to fabricate FETs. Such a direct transfer method avoids exposure of the sample to detrimental solvent processing as in a conventional lithographic process.

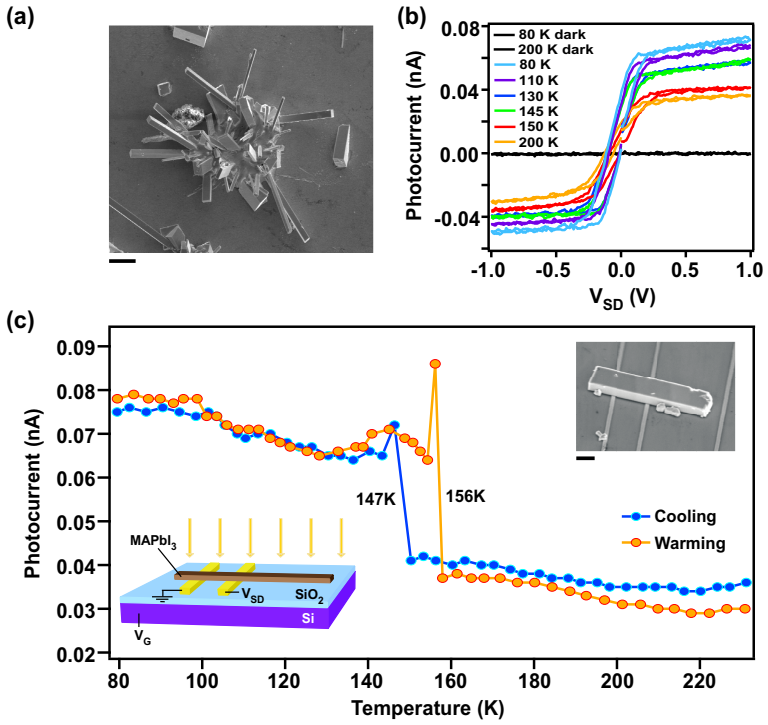

Figure 1: Photocurrent response across phase transition under global illumination. (a) Scanning electron microscopic (SEM) image of as-grown $MAPbI_3$ microcrystals. Scale bar represents 20 μm. (b) $I - V_{SD}$ curves at various temperatures in the dark and under 5×10^{-4} W / cm^2 global illumination. (c) Saturation photocurrent as a function of temperature with $V_{SD} = 1$ V and global illumination. The sample temperature is ramped slowly (3 K / min). Inset: left, Schematic of a $MAPbI_3$ microplate FET under global illumination; right, SEM image of microplate device. Scale bar represents 5 μm.

Under global illumination, the current first increases with source-drain bias (V_{SD}) then saturates as V_{SD} increases above 0.3 V (Figure 1b). The $I - V_{SD}$ characteristics can be understood by a back-to-back diode model.[24] The saturation current changes abruptly at 147 K (156 K) during cooling (warming) (Figure 1c). The photocurrent change shows a single step and occurs in only a few milliseconds (Figures S2 and S3 in Supporting Information), implying that the entire sample undergoes phase transition simultaneously without any mixed phase domains. This critical temperature T_c agrees well with the reported values for the tetragonal to orthorhombic phase transition.[18,25] The specific T_c values vary from device to device in a range of 15 K among the 10 devices we have measured to date, and are lower in thinner samples, as noticed in a previous work.[25] Interestingly, we have occasionally

observed a temporary photocurrent overshoot that occurs at the phase transition (Figure 1c), which may be related to the induced strain as the sample abruptly shrinks by 1 % from the tetragonal to orthorhombic phase.[26]

SPCM is then performed to extract carrier diffusion lengths.[17,18,20,24,27,28] The experimental setup is displayed in Figure 2b, where a microplate device is locally excited by a focused 532 nm CW laser with a diameter about 1 μm. While the laser is raster scanned across the entire device surface, the photo-induced current is recorded as a function of laser position and then plotted into 2D photocurrent maps (Figure 2a). At $V_{SD} = 0$ V, only very weak photocurrent is observed. At $V_{SD} = 3$ V, the enhanced band bending at the reversely biased contact leads to a much stronger photocurrent (Figure S4). The photocurrent is peaked near the negatively biased contact, indicating the material is n-type.

While the maximum external quantum efficiency (EQE, defined by the number of collected electrons over the number of incident photons) remains about 35% at all temperatures, the photo-response area sensitively depends on temperature. The laser generates photocurrent both inside and outside the channel, illustrating that the photoexcited carriers can diffuse from outside the channel to the electrodes. Above T_c, the photocurrent is only pronounced in the vicinity of the contacts. Below T_c, the active area in which laser can create photocurrent increases abruptly, which provides a microscopic understanding of the observed sudden photocurrent change under uniform illumination. At 80 K, the photocurrent remains nearly the same when the laser is scanned over the entire 90 μm long sample (Figure 2a,d), indicating that the locally generated carriers are equally capable of reaching the contacts and being collected, regardless of initial generation position.

Quantitatively, we extract photocurrent decay length L_D by fitting the photocurrent distributions along the microplate axis with a hyperbolic function $I(x_0) = I_0 \cosh[(x_0 - L)/L_D]$, where x_0 is distance between the laser position and the contact, and L is the length of microplate outside the channel. A cosh function is used instead of exponential when L_D is not small compared with L[29] (see math justification in Supporting Information). We only fit

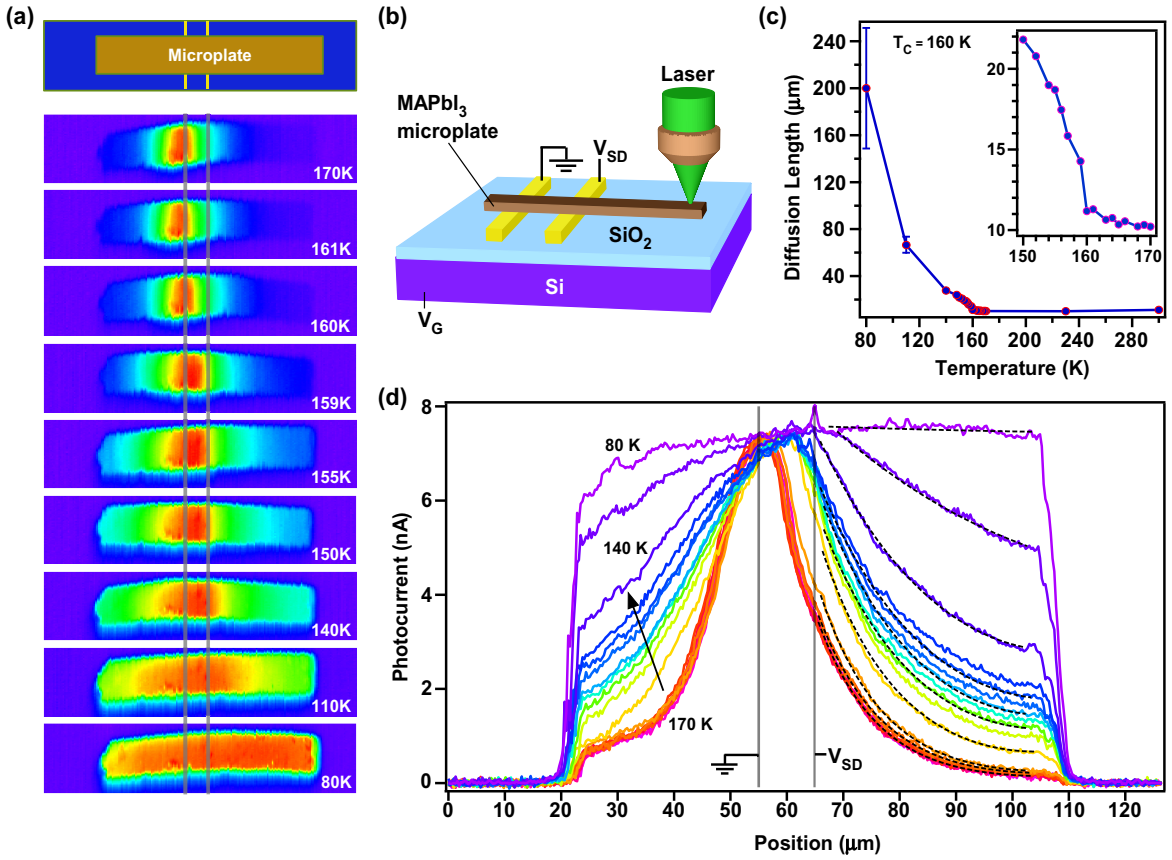

Figure 2: Spatially resolved photocurrent. (a) Device layout and photocurrent maps at various temperatures. Grey lines indicate electrode placement. (b) SPCM schematic. (c) Temperature dependent carrier diffusion length extracted by curve fitting photocurrent distributions in (d). Inset shows zoomed-in view of values in the vicinity of T_c (160 K). (d) Photocurrent profiles along the microplate axis at various temperatures, taken during warming process with 50 nW laser power and V_{SD} = 3 V. Grey vertical lines indicate electrode placement and black dashed curves are curve fittings.

photocurrent distribution outside the channel, to ensure diffusive transport of carriers[17] and determine L_{diff} from L_D. L_D values are similar on both sides of the channel and the slight difference is presumably caused by the variation in local defect density along the microplate. To rigorously confirm the accuracy of this method, we have simulated the photocurrent distributions, by performing a 2D cross-sectional modeling of perovskite devices under local photoexcitation using COMSOL Multiphysics.[24] The simulated photocurrent distributions follow nicely the experimental data (Figure S5). Fits using cosh function yield L_D in excellent agreement with L_{diff} calculated from the simulation parameters (Figure S5b).

The extracted L_D values remain about 10 μm above T_c, but rapidly increase to 22 μm as temperature decreases within 10 K below T_c (Figure 2c inset). At 80 K, L_D reaches 200 $\pm$ 50 μm. The large error bar at 80 K arises because of the finite sample length ($L < L_D$, see error analysis in the Supporting Information). L_D values at 80 K range from 100 - 200 μm depending on the sample (data for another sample is shown in Figure S6). Our result is different from a previous work,[18] where the hole diffusion length was found to be at maximum 150 μm at 160 K but decrease to 50 μm at 96 K. The reason for this discrepancy is unclear but is most likely related to the sample preparation. Our growth method yields samples with exceptionally low trap density, as demonstrated previously.[21,30–32]

Transient photocurrent measurements are then performed to obtain carrier lifetime at various temperatures (Figure S7 and Methods). The carrier lifetime increases from less than 0.5 μs (our temporal resolution limit) above T_c to about 2 μs at 80 K for the same device as in Figure 2. From this lifetime and the measured L_{diff}, we estimate a carrier mobility ($\mu = qL_{diff}^2/\tau k_B T$) of 3×10^4 cm^2 / V s at 80 K, which is one order of magnitude higher than the highest reported values[33,34] (Table S1). Lifetimes differ slightly across devices, ranging from <0.5 to 2 μs at 80 K (see diffusion length and lifetime measurements in another device in Figure S7b,d), but mobility values are consistently high, on the order of 10^4 - 10^5 cm^2/ V s at 80 K.

The observed highly non-local photocurrent indicates efficient transport of photogenerated charge carriers, which can generally be understood by four possible mechanisms: (a) photon recycling, (b) exciton polariton condensate, (c) free charge carrier diffusion, and (d) free exciton diffusion. We show that the first three mechanisms are unlikely. (a) Photon recycling via re-absorption/re-emission[35] is unlikely to account for the observed 200 μm photocurrent decay, as the optical loss through light escaping microplate surfaces alone would result in a maximum of 20 μm decay length according to our calculation (see Supporting Information), even when assuming unity photoluminescence efficiency. (b) Exciton polariton condensate[36] requires a microcavity structure to confine the light. Our microplate does not

have such a structure and optical loss would result in a short decay length. Free minority carrier diffusion, mechanism (c), appears plausible but demands a 400-fold increase in mobility to account for the rapid increase of L_D below T_c from 160 K to 80 K. Our molecular dynamics simulations of electron-phonon interactions and carrier effective masses (Supporting Information) show that this is inconsistent with the scaling expected for free carriers or charged polarons across the temperature range. Similarly, existing polaron models predict $\mu \sim T^{-1.5}$ and a mobility change of only a factor of 3 from 160 K to 80 K.[12]

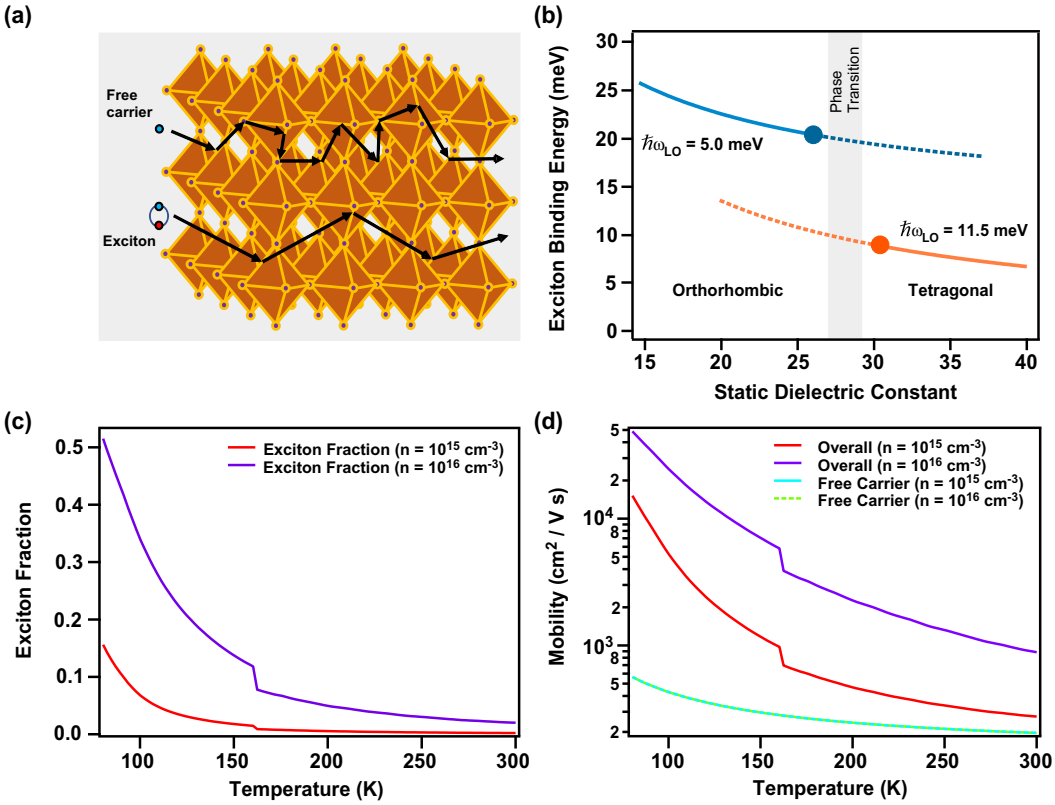

Figure 3: Calculation of free exciton and free carrier mobilities. (a) Visualization of free carrier versus exciton scattering in halide perovskites (scattering lengths not to scale). (b) Exciton binding energy, calculated taking into account polaronic effects, and as a function of static dielectric constant and LO phonon frequencies, which are phase-dependent. (c) Calculated exciton fraction as a function of temperature, at carrier densities $n = 10^{15}$ cm^{-3} and $n = 10^{16}$ cm^{-3}, showing significant exciton population at low temperatures. (d) Calculated free carrier mobility and overall mobility as a function of temperature. Free carrier mobility is independent of carrier density, while overall mobility is increased at higher densities due to higher exciton fractions.

The above consideration leads us to attribute the origin of the highly non-local pho-

tocurrent at low temperature to efficient exciton transport, mechanism (d). A relatively large value of exciton binding energy E_B (larger than 20 meV) in the orthorhombic phase discontinuously drops to below 10 meV at room temperature tetragonal phase.[37] This is fairly consistent with the value of 16 ± 2 meV found in the orthorhombic phase and a few meV in the tetragonal phase in $MAPbI_3$ by magnetic field dependent optical absorption.[38] Using an effective-interaction-potential model[39,40] (Supporting Information), we calculated the exciton binding energies of $MAPbI_3$ in good agreement with the measurements, 20.1 meV and 9.1 meV in the low and high temperature phases, respectively, as shown in Figure 3b. These excitonic binding energies suggest that excitons are unlikely to form at room temperature but they become significant at low temperatures. The exciton fraction over the total carriers is shown in Figure 3c, calculated following the approach in a previous report,[41] and using the temperature-dependent exciton binding energy.[37] The abrupt increase in exciton fraction across the phase transition is a result of phase-dependent exciton binding energies. Note that the exciton fraction sensitively depends on the total carrier density, as high carrier density promotes exciton formation. The total carrier density in our sample is on the order of 10^{15} - 10^{16} cm^{-3}, estimated from the laser power and carrier lifetime.

The rapid increase of mobility at low temperature can then be understood as the exponential increase of exciton fraction with decreasing temperature. In this exciton model, the record-high mobility indicated by the long L_D does not contradict the non-excitonic free carrier mobilities reported by earlier works. Even though an exciton is charge neutral, its mobility can be defined from its diffusion coefficient in analogy to charge by Einstein relation $\mu = qD/k_BT$. Charge neutral excitons create photocurrent when electron and hole pairs are separated as a result of band bending near the contact.

We hypothesize that the reason for the highly efficient exciton transport is the dipolar nature of excitons. Since dipole fields are shorter ranged than monopole fields, longitudinal optical (LO) phonons interact significantly less with excitons than with free carriers. Moreover, static ground-state excitonic dipoles do not exist in the centrosymmetric orthorhom-

bic phases, and can only be dynamically induced by other charge fluctuations such as LO phonons. As a result, the scattering of excitons is expected to be less frequent than that of free carriers or charged polarons. To estimate the relative scattering rates of free carriers and excitons, we consider the interaction strength of an induced excitonic dipole, given by the polarizability $\alpha = \frac{18a_0^3}{4}$ of an exciton within a hydrogenic model,[42] with LO phonon charge fluctuations. Here, a_0 is the exciton Bohr radius. Compared to the interaction between free carriers (holes) and LO phonons, we find that the exciton-LO phonon interaction strength, or probability amplitude for scattering, is reduced by a factor of $\sqrt{\gamma} = \left(\frac{\alpha}{\epsilon_\infty R_x^4}\right) / \left(\frac{1}{R_h}\right)$. Here, $R_h = \sqrt{\frac{\hbar}{2m_h\omega_{LO}}}$ and $R_x = \sqrt{\frac{\hbar}{2m_x\omega_{LO}}}$ are the hole and exciton polaron radii that characterize the length scales of LO fluctuations around these species, with masses m_h and m_x respectively. The scattering rate, or probability, is therefore reduced by a factor of $\gamma = \left(\frac{18a_0^3 R_h}{4\epsilon_\infty R_x^4}\right)^2$. Using typical values for $MAPbI_3$ (see Supporting Information), we find that exciton scattering from LO phonons is reduced by a factor of $\gamma = 5 \times 10^{-4}$. This is a lower bound for γ, as other scattering mechanisms could be present for excitons. In Figure 3d, we plot the overall mobility, weighted by free carrier and excitonic contributions. The free-carrier mobility is calculated using the Kadanoff mobility,[12] while the exciton mobility was taken to be larger by a factor of $1/\gamma$. In Figure 3d, we show that reduced excitonic scattering at the value of $\gamma = 6 \times 10^{-3}$, leads to increases in low-temperature mobility comparable to measured values in our devices.

Finally, we present the field effect on carrier diffusion in halide perovskite microplate FETs. In the dark, the conductance increases at positive V_G indicating the device is n-type (Figures 4a and S8). The gate dependence shows significant hysteresis at room temperature as explained by gate induced ion migration.[22] The hysteresis is greatly reduced at lower temperature, as ion migration is suppressed. By assuming a parallel plate capacitance (a combination of vacuum gap and oxide layer), an apparent field-effect mobility on the order of 0.01 cm^2 / V s can be extracted from the gate dependence at 80 K (Figure 4a). This apparent mobility value does not represent the real carrier mobility of the material because

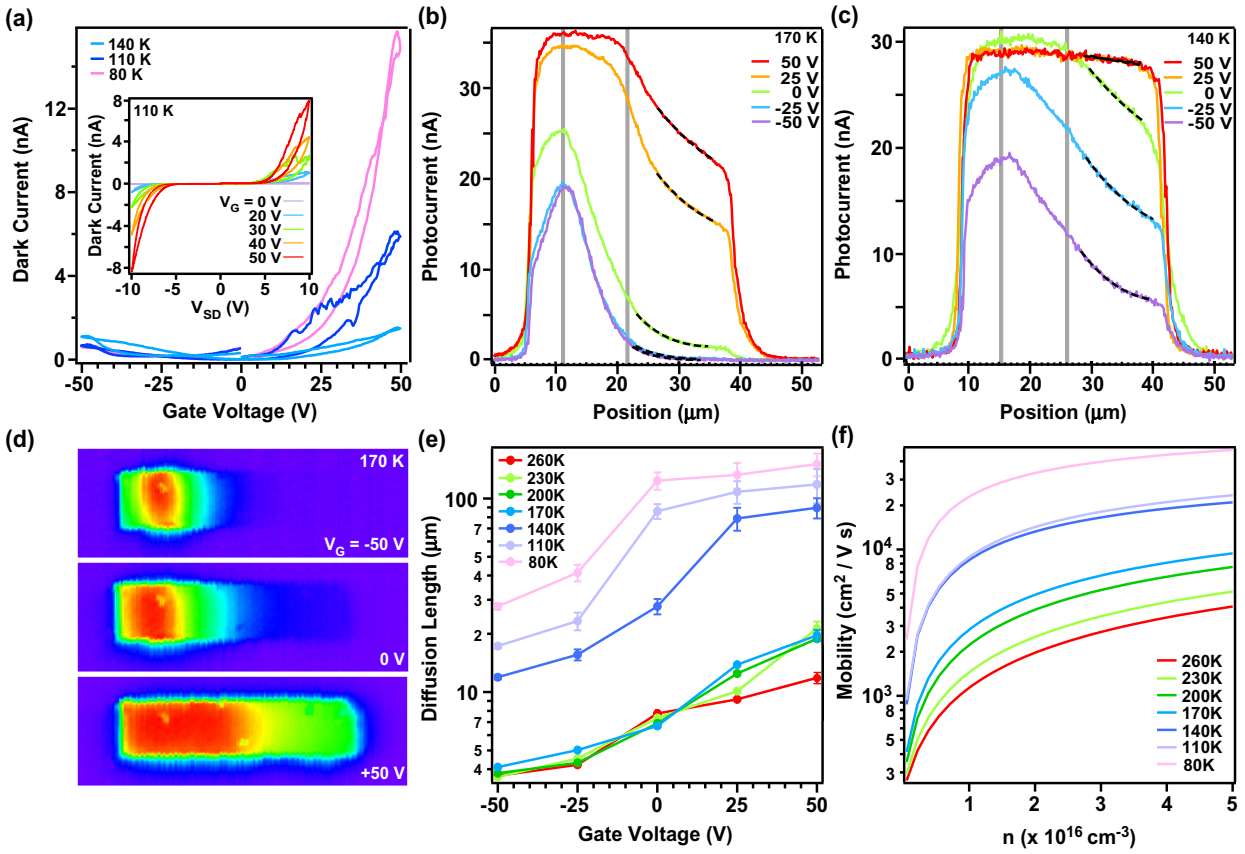

Figure 4: Field effect on carrier diffusion. (a) Dark current as a function of V_G at fixed $V_{SD} = 10$ V and various temperatures. Inset: Dark $I - V_{SD}$ curves at various V_G at 110 K. (b) and (c) show SPCM profiles with varying gate voltage and fixed bias of 1.5 V at 170 K (tetragonal phase) and 140 K (orthorhombic phase), respectively. Grey vertical lines indicate electrode placement. (d) Normalized photocurrent maps showing diffusion enhancement (suppression) at positive (negative) gate voltage at 170 K. (e) Carrier diffusion length at various temperatures as a function of gate voltage. (f) Simulated mobility values as a function of overall carrier density at various temperatures.

of large contact barriers evidenced by the nonlinear $I - V_{SD}$ curves (Figure 4a inset and Figure S9). Furthermore, this low mobility value does not contradict with the high mobility value indicated by the long photocurrent decay length, as the gate dependence measures the mobility for free carriers or charged polarons instead of excitons.

Photocurrent distributions sensitively depend on V_G (Figure 4b-d). At positive V_G, the photocurrent magnitude increases, likely caused by the reduced sample resistance and/or enhanced band bending at contact. The carrier diffusion length also significantly depends on the gate voltage, changing by a factor of 8 at low temperature as V_G varies from -50 V

to 50 V (Figure 4e). Such a strong electric field control of carrier diffusion has not been reported before in halide perovskites. We consistently observe that L_D increases (decreases) at positive (negative) V_G. In the n-type device, this trend indicates that increasing the majority carrier (electron) concentration enhances the diffusion of the minority carrier (hole) or exciton. This behavior cannot be understood by the lifetime reduction at high majority carrier density as in other semiconductor nano-devices.[43,44] Instead, this unusual gate dependence is consistent with the exciton model. The higher carrier concentration at positive V_G increases the probability of exciton formation, leading to a larger exciton fraction and hence higher overall mobility (Figure 3). The calculated mobility values taking into account exciton formation (Figure 4f) follow well the general trend of the experimental results.

In summary, we have observed temperature and gate dependent carrier diffusion in single-crystal $MAPbI_3$ microstructures. L_D remains about 10 μm in the tetragonal phase, but increases sharply to 200 μm at 80 K in the orthorhombic phase. L_D also increases with majority carrier (electron) concentration tuned by gate voltage. The rapid increase of L_D can be understood by formation and efficient transport of excitons at low temperature. The phonon-scattering rate of excitons is significantly suppressed as a consequence of their dipolar nature, compared to free carriers and charged polarons. This hypothesis is supported by calculated temperature and carrier concentration dependent mobilities that are in excellent agreement with the experimental results. Though the relatively low excitonic binding energy in $MAPbI_3$ suggests that excitonic effects only become important at low temperature in this material, excitons are expected to play a significant role at room temperature in low dimensional halide perovskites.[45,46] Our work provides valuable insight on understanding the interplay among free carriers, excitons, and phonons in the halide perovskite materials.

Methods

Microstructure growth and device fabrication. 40 mg of MAI powder (Sigma Aldrich >98%) was slowly dissolved in 1 mL of isopropyl alcohol (IPA 99.5%) in a glass vial inside a nitrogen glovebox. Meanwhile 100 mg of $PbAc_2$ $3H_2O$ (Sigma Aldrich 99.999%) powder was dissolved in 1 mL of deionized water. The $PbAc_2$ solution was distributed across the FTO-coated glass slides by spin-coating at 600 RPM for 40 seconds. The coated substrate was baked at 60 °C until dry and then placed upside down inside the vial of MAI solution at 50 °C for several days. Afterwards, the substrate was gently dipped into IPA for a few seconds, and then blown dry with nitrogen. The as-grown microstructures were then mechanically transferred via a microfiber to 300 nm SiO_2 covered Si substrates with pre-patterned 10 nm Cr/ 30 nm Au electrodes, to achieve single microplate FETs.

Optoelectronic measurements. All measurements were performed in an optical cryostat (Janis ST-500) with a pressure of 10^{-6} torr. Current-voltage curves were measured through a current preamplifier (DL Instruments, model 1211) and a NI data acquisition system. SPCM measurements were performed using a home-built setup based upon an Olympus microscope. A 532 nm CW laser was focused by a 40x objective lens to a diffraction limited spot about 1 μm and raster scanned on a planar microstructure device by a pair of mirrors mounted on galvanometers to produce 2D photocurrent maps. For transient photocurrent measurements, we used a photoelastic modulator (Figure S7a) to modulate the light intensity at 50 kHz with a light intensity decay time about 0.5 μs (see more in Supporting Information).

Electronic structure dynamics calculations. We investigate the effect of temperature dependent band structure fluctuations on free carrier mobility using simulations of atomic and electronic structure dynamics. Atomic motion is simulated using classical molecular dynamics (MD) with a force field by Mattoni et al.[47] at 10 temperatures between 100 K and 300 K. Atomic positions are extracted every 30 fs over a 30 ps trajectory and used to calculate electronic structure using a modified version of the tight binding model by Mayers

et al.,[13] in which onsite orbital energies are modified using both the Coulomb potential and its second derivative.

ASSOCIATED CONTENT

Supporting Information

The Supporting Information is available free of charge on the ACS Publications website at DOI: xxx.

Analytic justification of SPCM extraction of carrier diffusion length by SPCM; COMSOL device simulation for SPCM profiles; error analysis; data on abrupt photocurrent change across phase transition; band bending diagrams and bias dependent SPCM results; temperature dependent SPCM results in a different device; transient photocurrent measurement setup and results; gate dependent dark conductance at various temperatures; estimation of photocurrent decay length via photon recycling; MD simulation approach and results; calculation of exciton binding energies; and X-ray diffraction data for $MAPbI_3$ microstructures.

AUTHOR INFORMATION

Corresponding Authors

*E-mail: yu@physics.ucdavis.edu.

ORCID

Dong Yu: 0000-0002-8386-065X

R. T. Senger: 0000-0003-0800-1924

Liang Z. Tan: 0000-0003-4724-6369

Notes

The authors declare that they have no competing financial interests.

ACKNOWLEDGEMENT

This work was supported by the U.S. National Science Foundation Grants DMR-1710737 and DMR-1838532. Device fabrication was partially carried out at the Molecular Foundry, and L.Z.T. was supported by the Molecular Foundry, which is funded by the Office of Science, Office of Basic Energy Sciences, of the U.S. Department of Energy under Contract No. DE-AC02-05CH11231. D.A. was supported by the Computational Materials Sciences Program funded by the US Department of Energy, Office of Science, Basic Energy Sciences, Materials Sciences and Engineering Division. Y.F. and S.J. thank the support by the US Department of Energy, Office of Basic Energy Sciences, Division of Materials Sciences and Engineering, under award DE-FG02-09ER46664. R.T.S. acknowledges the support from The Turkish Fulbright Commission Visiting Scholar Program.

References

(1) Yaffe, O.; Guo, Y.; Tan, L. Z.; Egger, D. A.; Hull, T.; Stoumpos, C. C.; Zheng, F.; Heinz, T. F.; Kronik, L.; Kanatzidis, M. G. et al. Local polar fluctuations in lead halide perovskite crystals. *Phys. Rev. Lett.* **2017**, *118*, 136001.

(2) Miyata, K.; Atallah, T. L.; Zhu, X.-Y. Lead halide perovskites: Crystal-liquid duality, phonon glass electron crystals, and large polaron formation. *Sci. Adv.* **2017**, *3*, e1701469.

(3) Zheng, F.; Tan, L. Z.; Liu, S.; Rappe, A. M. Rashba spin–orbit coupling enhanced carrier lifetime in CH3NH3PbI3. *Nano Lett.* **2015**, *15*, 7794–7800.

(4) Yuan, Y.; Huang, J. Ion migration in organometal trihalide perovskite and its impact on photovoltaic efficiency and stability. *Acc. Chem. Res.* **2016**, *49*, 286–293.

(5) Rakita, Y.; Bar-Elli, O.; Meirzadeh, E.; Kaslasi, H.; Peleg, Y.; Hodes, G.; Lubomirsky, I.; Oron, D.; Ehre, D.; Cahen, D. Tetragonal CH3NH3PbI3 is ferroelectric. *Proc. Natl. Acad. Sci.* **2017**, *114*, E5504–E5512.

(6) Karakus, M.; Jensen, S. A.; D'Angelo, F.; Turchinovich, D.; Bonn, M.; Canovas, E. Phonon–electron scattering limits free charge mobility in methylammonium lead iodide perovskites. *J. Phys. Chem. Lett.* **2015**, *6*, 4991–4996.

(7) Savenije, T. J.; Ponseca Jr, C. S.; Kunneman, L.; Abdellah, M.; Zheng, K.; Tian, Y.; Zhu, Q.; Canton, S. E.; Scheblykin, I. G.; Pullerits, T. et al. Thermally activated exciton dissociation and recombination control the carrier dynamics in organometal halide perovskite. *J. Phys. Chem. Lett.* **2014**, *5*, 2189–2194.

(8) Yi, H. T.; Wu, X.; Zhu, X.; Podzorov, V. Intrinsic Charge Transport across Phase Transitions in Hybrid Organo-Inorganic Perovskites. *Adv. Mater.* **2016**, *28*, 6509–6514.

(9) Devreese, J. T.; Alexandrov, A. S. Fröhlich polaron and bipolaron: recent developments. *Rep. Prog. Phys.* **2009**, *72*, 066501.

(10) Sendner, M.; Nayak, P. K.; Egger, D. A.; Beck, S.; Müller, C.; Epding, B.; Kowalsky, W.; Kronik, L.; Snaith, H. J.; Pucci, A. et al. Optical phonons in methylammonium lead halide perovskites and implications for charge transport. *Mater. Horiz.* **2016**, *3*, 613–620.

(11) Filippetti, A.; Mattoni, A.; Caddeo, C.; Saba, M. I.; Delugas, P. Low electron-polar optical phonon scattering as a fundamental aspect of carrier mobility in methylammonium lead halide CH3NH3PbI3 perovskites. *Phys. Chem. Chem. Phys.* **2016**, *18*, 15352–15362.

(12) Frost, J. M. Calculating polaron mobility in halide perovskites. *Phys. Rev. B* **2017**, *96*, 195202.

(13) Mayers, M. Z.; Tan, L. Z.; Egger, D. A.; Rappe, A. M.; Reichman, D. R. How Lattice and Charge Fluctuations Control Carrier Dynamics in Halide Perovskites. *Nano Lett.* **2018**, *18*, 8041–8046, PMID: 30387614.

(14) Stranks, S. D.; Eperon, G. E.; Grancini, G.; Menelaou, C.; Alcocer, M. J.; Leijtens, T.; Herz, L. M.; Petrozza, A.; Snaith, H. J. Electron-hole diffusion lengths exceeding 1 micrometer in an organometal trihalide perovskite absorber. *Science* **2013**, *342*, 341–344.

(15) Dong, Q.; Fang, Y.; Shao, Y.; Mulligan, P.; Qiu, J.; Cao, L.; Huang, J. Electron-hole diffusion lengths¿ 175 μm in solution-grown CH3NH3PbI3 single crystals. *Science* **2015**, *347*, 967–970.

(16) Hu, X.; Wang, X.; Fan, P.; Li, Y.; Zhang, X.; Liu, Q.; Zheng, W.; Xu, G.; Wang, X.; Zhu, X. et al. Visualizing carrier transport in metal halide perovskite nanoplates via electric field modulated photoluminescence imaging. *Nano Lett.* **2018**, *18*, 3024–3031.

(17) Xiao, R.; Hou, Y.; Fu, Y.; Peng, X.; Wang, Q.; Gonzalez, E.; Jin, S.; Yu, D. Photocurrent Mapping in Single-Crystal Methylammonium Lead Iodide Perovskite Nanostructures. *Nano Lett.* **2016**, *16*, 7710–7717.

(18) Semonin, O. E.; Elbaz, G. A.; Straus, D. B.; Hull, T. D.; Paley, D. W.; Van der Zande, A. M.; Hone, J. C.; Kymissis, I.; Kagan, C. R.; Roy, X. et al. Limits of carrier diffusion in N-type and P-type CH3NH3PbI3 perovskite single crystals. *J. Phys. Chem. Lett.* **2016**, *7*, 3510–3518.

(19) Liu, S.; Wang, L.; Lin, W.-C.; Sucharitakul, S.; Burda, C.; Gao, X. P. Imaging the long transport lengths of photo-generated carriers in oriented perovskite films. *Nano Lett.* **2016**, *16*, 7925–7929.

(20) Wang, X.; Ling, Y.; Chiu, Y.-C.; Du, Y.; Barreda, J. L.; Perez-Orive, F.; Ma, B.; Xiong, P.; Gao, H. Dynamic Electronic Junctions in Organic–Inorganic Hybrid Perovskites. *Nano Lett.* **2017**, *17*, 4831–4839.

(21) Fu, Y.; Zhu, H.; Chen, J.; Hautzinger, M. P.; Zhu, X.-Y.; Jin, S. Metal halide perovskite nanostructures for optoelectronic applications and the study of physical properties. *Na. Rev. Mater.* **2019**, 1.

(22) Chin, X. Y.; Cortecchia, D.; Yin, J.; Bruno, A.; Soci, C. Lead iodide perovskite light-emitting field-effect transistor. *Nat. Commun.* **2015**, *6*, 7383.

(23) Fu, Y.; Meng, F.; Rowley, M. B.; Thompson, B. J.; Shearer, M. J.; Ma, D.; Hamers, R. J.; Wright, J. C.; Jin, S. Solution growth of single crystal methylammonium lead halide perovskite nanostructures for optoelectronic and photovoltaic applications. *J. Am. Chem. Soc.* **2015**, *137*, 5810–5818.

(24) Xiao, R.; Hou, Y.; Law, M.; Yu, D. On the Use of Photocurrent Imaging To Determine Carrier Diffusion Lengths in Nanostructured Thin-Film Field-Effect Transistors. *J. Phys. Chem. C* **2018**, *122*, 18356–18364.

(25) Li, D.; Wang, G.; Cheng, H.-C.; Chen, C.-Y.; Wu, H.; Liu, Y.; Huang, Y.; Duan, X. Size-dependent phase transition in methylammonium lead iodide perovskite microplate crystals. *Nat. Commun.* **2016**, *7*, 11330.

(26) Keshavarz, M.; Ottesen, M.; Wiedmann, S.; Wharmby, M.; Küchler, R.; Yuan, H.; Debroye, E.; Steele, J. A.; Martens, J.; Hussey, N. E. et al. Tracking Structural Phase Transitions in Lead-Halide Perovskites by Means of Thermal Expansion. *Adv. Mater.* **2019**, *31*, 1900521.

(27) Graham, R.; Yu, D. Scanning photocurrent microscopy in semiconductor nanostructures. *Mod. Phys. Lett. B* **2013**, *27*, 1330018.

(28) Fu, D.; Zou, J.; Wang, K.; Zhang, R.; Yu, D.; Wu, J. Electrothermal dynamics of semiconductor nanowires under local carrier modulation. *Nano Lett.* **2011**, *11*, 3809–3815.

(29) Hou, Y.; Wang, R.; Xiao, R.; McClintock, L.; Travaglini, H. C.; Francia, J. P.; Fetsch, H.; Erten, O.; Savrasov, S. Y.; Wang, B. et al. Millimetre-long transport of photogenerated carriers in topological insulators. *Nature Communications* **2019**, *10*, 1–7.

(30) Zhu, H.; Fu, Y.; Meng, F.; Wu, X.; Gong, Z.; Ding, Q.; Gustafsson, M. V.; Trinh, M. T.; Jin, S.; Zhu, X. Lead halide perovskite nanowire lasers with low lasing thresholds and high quality factors. *Nat. Mater.* **2015**, *14*, 636.

(31) Zhu, H.; Miyata, K.; Fu, Y.; Wang, J.; Joshi, P. P.; Niesner, D.; Williams, K. W.; Jin, S.; Zhu, X.-Y. Screening in crystalline liquids protects energetic carriers in hybrid perovskites. *Science* **2016**, *353*, 1409–1413.

(32) Zhu, H.; Trinh, M. T.; Wang, J.; Fu, Y.; Joshi, P. P.; Miyata, K.; Jin, S.; Zhu, X.-Y. Organic cations might not be essential to the remarkable properties of band edge carriers in lead halide perovskites. *Adv. Mater.* **2017**, *29*, 1603072.

(33) La-o vorakiat, C.; Xia, H.; Kadro, J.; Salim, T.; Zhao, D.; Ahmed, T.; Lam, Y. M.; Zhu, J.-X.; Marcus, R. A.; Michel-Beyerle, M.-E. et al. Phonon mode transformation across the orthohombic–tetragonal phase transition in a lead iodide perovskite CH3NH3PbI3: a terahertz time-domain spectroscopy approach. *J. Phys. Chem. Lett.* **2015**, *7*, 1–6.

(34) Shrestha, S.; Matt, G. J.; Osvet, A.; Niesner, D.; Hock, R.; Brabec, C. J. Assessing Temperature Dependence of Drift Mobility in Methylammonium Lead Iodide Perovskite Single Crystals. *J. Phys. Chem. C* **2018**, *122*, 5935–5939.

(35) Pazos-Outón, L. M.; Szumilo, M.; Lamboll, R.; Richter, J. M.; Crespo-Quesada, M.; Abdi-Jalebi, M.; Beeson, H. J.; Vrućinić, M.; Alsari, M.; Snaith, H. J. et al. Photon recycling in lead iodide perovskite solar cells. *Science* **2016**, *351*, 1430–1433.

(36) Su, R.; Wang, J.; Zhao, J.; Xing, J.; Zhao, W.; Diederichs, C.; Liew, T. C.; Xiong, Q. Room temperature long-range coherent exciton polariton condensate flow in lead halide perovskites. *Sci. Adv.* **2018**, *4*, eaau0244.

(37) Davies, C. L.; Filip, M. R.; Patel, J. B.; Crothers, T. W.; Verdi, C.; Wright, A. D.; Milot, R. L.; Giustino, F.; Johnston, M. B.; Herz, L. M. Bimolecular recombination in methylammonium lead triiodide perovskite is an inverse absorption process. *Nat. Commun.* **2018**, *9*, 293.

(38) Miyata, A.; Mitioglu, A.; Plochocka, P.; Portugall, O.; Wang, J. T.-W.; Stranks, S. D.; Snaith, H. J.; Nicholas, R. J. Direct measurement of the exciton binding energy and effective masses for charge carriers in organic-inorganic tri-halide perovskites. *Nat. Phys.* **2015**, *11*, 582–587.

(39) Pollmann, J.; Büttner, H. Effective Hamiltonians and binding energies of Wannier excitons in polar semiconductors. *Phys. Rev. B* **1977**, *16*, 4480–4490.

(40) Senger, R. T.; Bajaj, K. K. Optical properties of confined polaronic excitons in spherical ionic quantum dots. *Phys. Rev. B* **2003**, *68*, 045313.

(41) D'innocenzo, V.; Grancini, G.; Alcocer, M. J.; Kandada, A. R. S.; Stranks, S. D.; Lee, M. M.; Lanzani, G.; Snaith, H. J.; Petrozza, A. Excitons versus free charges in organo-lead tri-halide perovskites. *Nat. Commun.* **2014**, *5*, 3586.

(42) Bowers, W. A. The classical polarizability of the hydrogen atom. *Am. J. Phys.* **1986**, *54*, 347–350.

(43) Yang, Y.; Li, J.; Wu, H.; Oh, E.; Yu, D. Controlled ambipolar doping and gate voltage dependent carrier diffusion length in lead sulfide nanowires. *Nano Lett.* **2012**, *12*, 5890–5896.

(44) Otto, T.; Miller, C.; Tolentino, J.; Liu, Y.; Law, M.; Yu, D. Gate-dependent carrier diffusion length in lead selenide quantum dot field-effect transistors. *Nano letters* **2013**, *13*, 3463–3469.

(45) Cao, D. H.; Stoumpos, C. C.; Farha, O. K.; Hupp, J. T.; Kanatzidis, M. G. 2D homologous perovskites as light-absorbing materials for solar cell applications. *J. Am. Chem. Soc.* **2015**, *137*, 7843–7850.

(46) Yuan, Z.; Zhou, C.; Tian, Y.; Shu, Y.; Messier, J.; Wang, J. C.; Van De Burgt, L. J.; Kountouriotis, K.; Xin, Y.; Holt, E. et al. One-dimensional organic lead halide perovskites with efficient bluish white-light emission. *Nat. commun.* **2017**, *8*, 14051.

(47) Mattoni, A.; Filippetti, A.; Saba, M. I.; Delugas, P. Methylammonium Rotational Dynamics in Lead Halide Perovskite by Classical Molecular Dynamics: The Role of Temperature. *J. Phys. Chem. C* **2015**, *119*, 17421–17428.